



Modulating the photooxidation selectivity on graphitic carbon nitride by tuning edge functional groups



Shasha Li ^{a,b}, Yufan Zhang ^{a,b}, Youji Li ^c, Jing Xue ^{a,b}, Chaoyuan Deng ^{a,b}, Wenjing Song ^{a,b}, Chuncheng Chen ^{a,b,*}, Jincai Zhao ^{a,b}

^a Key Laboratory of Photochemistry, Beijing National Laboratory for Molecular Sciences, Institute of Chemistry, Chinese Academy of Sciences, Beijing 100190, PR China

^b University of Chinese Academy of Sciences, Beijing 100049, PR China

^c College of Chemistry and Chemical Engineering, Jishou University, Jishou 416000, PR China

ARTICLE INFO

Keywords:

Photocatalysis
Polymeric carbon nitride
Functional groups engineering
Selective oxidation
 CH_3SH

ABSTRACT

Selective photooxidation reactions offer a promising route for transformation of organic pollutants into high-value products under mild conditions. In this work, we demonstrate that the edge functional groups in polymer carbon nitride (PCN) were key to the selectivity of methyl mercaptan (CH_3SH) photocatalytic oxidation. The amino-decorated PCN favors the oxidation of the -SH group of CH_3SH to forming $\text{CH}_3\text{SO}_3\text{H}$ with selectivity up to 84.0%, while cyanamide-enriched PCN prefers to breaking the - CH_3 end of CH_3SH and produce H_2SO_4 with selectivity of 82.0%. The totally difference in reaction sites is ascribed to the functional-group-modulated electronic structure of PCN, which determines activity of photoinduced carriers and the molecular oxygen activation pathway. The amino- and cyanamide-decorated PCN leads to preferential generation of $^1\text{O}_2$ and O_2^- , respectively. This study highlights the significant role of edge groups engineering in modulation of the excitonic effects in PCN and the resultant selectivity control during photocatalytic reaction.

1. Introduction

Semiconductor-based photocatalytic solar-energy conversion technology, as an environmentally benign method, has been widely studied in the oxidation of volatile organic compounds [1,2]. Among various semiconductor photocatalysts, polymeric carbon nitride (PCN) has attracted tremendous attention as an emerging and promising metal-free photocatalyst with distinctive merits including facile synthesis, abundant availability, tunable structure, visible light absorption and robust chemical stability [3,4]. At present, most studies on PCN are centered at the development of new PCN materials to realize high photocatalytic efficiency. However, there are lack of strategies to control the reaction pathway to produce desirable products with high selectivity. Actually, only a few studies were reported to control the selectivity of photocatalytic reaction over PCN by varying external parameters or modifying with transition metal. For instance, the excitation wavelength was found to be able to tune the enantioselectivity of ethylbenzene oxidation to phenylethanol or the selective syntheses of a series of azo- and azoxy-aromatic compounds from nitroaromatics [5,6]. The coordination

environments of Cu incorporated in PCN was also found to change the products (CH_3OH or CO) of CO_2 reduction [7].

It is well-established that PCN materials exhibit a high density of defect sites, which is able to be functionalized. Theoretical and experimental evidence have demonstrated that edge-selective functionalization enables the regulation of various properties in PCN, such as photon absorption and electronic properties [8,9]. Accordingly, engineering the edge functional groups in PCN has been used to improve the photocatalytic efficiency for the evolution of H_2 and pollutants removal in previous studies [10–12]. These intriguing features in PCN by altering the dangling edge functional groups also provide a promising opportunity to modulate chemoselectivity of the photocatalytic reaction. However, photocatalytic selective oxidation modulated by edge functionalization is less explored, let alone a mechanistic understanding on how specific structural features in PCN affect selectivity. Such information is crucial for the rational design of functional PCN catalysts to regulate the reaction pathways assuring the final desired products.

Methyl mercaptan (CH_3SH), widely emitted from industry wastes, sewage/wastewater treatment plants, and sanitary landfill, is one of the

* Corresponding author at: Key Laboratory of Photochemistry, Beijing National Laboratory for Molecular Sciences, Institute of Chemistry, Chinese Academy of Sciences, Beijing 100190, PR China.

E-mail address: ccchen@iccas.ac.cn (C. Chen).

major causes that lead to the severe environmental malodorous pollution [13–16]. As a typical sulfur-containing volatile compounds, methyl mercaptan has an extremely low odor threshold of 0.4 ppb/v [17]. Besides its high toxicity and pathogenicity, methyl mercaptan is also reported to be involved in the physicochemical and photochemical processes of atmospheric sulfate aerosols [18,19]. Therefore, efficient elimination of CH₃SH pollution is of great significance for health and environment.

Over the past decades, many efforts have been devoted to CH₃SH abatement. Compared with traditional catalytic incineration, chemical scrubbing, and adsorption [20–25], catalytic oxidation technology is considered as a promising approach for CH₃SH removal, because of its less energy expenditure, simple operation, and minimal secondary pollution. During the catalytic oxidation of CH₃SH, CH₃SO₃H and H₂SO₄ are usually two major products. Both of them are important chemicals that can be used as feedstock or basic building blocks in fine chemical industry and energy storage [26,27]. Thus, it is highly attractive to regulate the CH₃SH oxidation reaction path to produce desired chemicals. In the previous studies, the oxidation of CH₃SH is generally reported to undergo a sequential manner, in which the CH₃SH is first oxidized to CH₃SO₃H, and subsequently to H₂SO₄ [28–31]. As a result, controlling the reaction process to stop at the CH₃SO₃H is a great challenge. To the best of our knowledge, the reported selectivity for CH₃SO₃H is less than 40% [28,29]. On the other hand, the complete transformation of CH₃SH to H₂SO₄ is also difficult, because of the inertness of CH₃SO₃H. Only under harsh conditions, such as using strong oxidants (O₃ or H₂O₂) and transitional/noble metal-based catalyst, can H₂SO₄ yield be increased [28,29,32,33].

The oxidation of CH₃SH can proceed theoretically through two pathways, either breaking the methyl group to directly deliver the H₂SO₄ products (CH₃SH→H₂SO₄), or oxidizing S site in CH₃SH yielding CH₃SO₃H (CH₃SH→CH₃SO₃H). Regulation of the reaction pathway would enable the selective formation of H₂SO₄ or CH₃SO₃H. In this study, we show that tuning the edge functional groups of PCN can direct the CH₃SH photooxidation along a desired reaction pathway, at similar polymer backbone and crystallinity of PCN. On amino-decorated PCN, the oxidation of S site is dominant, and the methyl group remains untouched, while the cyanamide-PCN tends to destroy the methyl group. Detailed comparisons in the structure, photoluminescence and formation of active oxygen species between these two photocatalysts were further carried out to provide deep insight into their different photocatalytic behaviors.

2. Experimental section

2.1. Preparation of photocatalysts

The synthesis of PCN-MT with melamine and trichloroisocyanuric acid refers to the work from Xie et al. [34] and Chen et al. [35] who prepared PCN using melamine-cyanuric chloride and melamine-cyanuric acid, respectively. Typically, melamine and trichloroisocyanuric acid (1:2 molar ratio) were mixed with 150 mL methanol solvent, and magnetically stirred at room temperature for about 12 h to obtain dried powders. The dry precursor was washed several times with methanol and deionized water, and then transferred to a vacuum oven at 60 °C overnight. The resulting powders were placed in a muffle furnace and calcined at 550 °C for 5 h with a ramp rate of 4.8 °C/min. The resultant samples were ground, affording yellow powders of PCN-MT.

PCN-IT was prepared through a modified ionothermal polymerization method according to previous reports [36]. Typically, 0.6 g of the PCN-MT sample was completely ground with KCl (3.3 g) and LiCl (2.7 g). The mixture was placed in a tube furnace and heated to 550 °C for 4 h at a rate of 4.8 °C/min in an argon atmosphere. The yellow green product was washed several times with boiling deionized water and then dried at 60 °C under vacuum.

PCN-NH₂ (Melamine), PCN-NH₂ (Dicyandiamide), PCN-NH₂ (Urea) were prepared by directly heating different precursors (melamine, dicyandiamide and urea) to 550 °C for 5 h with temperature ramping rate of 4.8 °C/min, respectively.

PCN-MT-xCN was synthesized according to previous reports [37]. Typically, 60 mg PCN-MT and 0 mmol, 0.5 mmol and 2 mmol of NaSCN (PCN-MT-0CN, PCN-MT-1CN, PCN-MT-2CN) were mixed with 13 mL acetonitrile in a 20 mL photoreactor, and magnetically stirred under white LED with energy density of 100 mW cm⁻² for 8 h. The resultant product was washed with methanol and deionized water for several times.

2.2. Characterization

XRD patterns were collected on an X-ray diffractometer (Empyrean, PANalytical) operating with a Cu K α X-ray source at a scan rate of 2°/min. FTIR spectra were acquired on a Nicolet iS50 FTIR spectrometer in a KBr pellet. The XPS were recorded on a Thermal ESCALAB 250Xi spectrometer with a Mg K α (1253.6 eV) source. All binding energies were corrected with respect to the C 1 s peak at 284.8 eV. The UV-vis diffuse reflectance spectra (DRS) of the samples were recorded on a UV-vis spectrophotometer (HITACHI UH-4150). The steady-state photoluminescence spectra, time-resolved photoluminescence spectra as well as the temperature dependent photoluminescence spectra were obtained on a FLS 1000 fluorescence spectrometer with an excitation wavelength of 374 nm. The reactive species on the photocatalysts were detected by a Bruker E500 electron paramagnetic resonance spectroscopy. 2,2,6,6-tetramethyl-4-piperidone (TEMP) and 5,5-Dimethyl-1-pyrroline-N-oxide (DMPO) were taken as spin-trapped reagents to identify $^1\text{O}_2$ and $\cdot\text{O}_2$, respectively. The electrochemical measurements were carried out on an Autolab PGSTAT302N electrochemical workstation equipped with a three-electrode system. Specifically, Ag/AgCl electrode, Pt wire and photocatalysts-coated FTO were employed as the reference electrode, the counter electrode, and the working electrode, respectively. The working electrode was prepared by coating a 200 μL slurry with 2 mg catalysts, 16 μL 5% Nafion and 184 μL ethanol onto the FTO (2 cm²). A xenon lamp (300 W) with AM 1.5 G cutoff filter was utilized as the light source. The electrolyte was a 0.25 M Na₂SO₄ solution.

2.3. Photocatalytic oxidation of CH₃SH

Photocatalytic oxidation of CH₃SH by PCN was carried out in a continuous flow stainless steel reactor (Beijing CEAuLight Co., Ltd., SUS304, diameter 106 mm, depth 78 mm) with a cover window of quartz (diameter 52 mm) at room temperature (25 °C) and atmospheric pressure. A 300 W xenon lamp (AM 1.5 G cutoff filter, light intensity 250 mW cm⁻²) as the light source was placed vertically on the top of the reactor. Photocatalysts were immobilized on quartz microfiber films (diameter, 5.2 cm) before the experiment. Typically, 50 mg PCN was ultrasonically dispersed in 8 mL methanol. Then the mixture was deposited onto the quartz microfiber films by drop-casting and dried in fume cupboard overnight. The inlet CH₃SH with an initial concentration of 50 ppm was prepared by diluting 500 ppm CH₃SH with synthetic air in a gas mixing chamber under dry conditions. The total flow rate was controlled at 50 mL min⁻¹ using mass flow controllers. Before the reaction, 50 ppm CH₃SH was passed through the PCN catalysts in the dark for 30 min to reach adsorption–desorption equilibrium. The concentration of CH₃SH and oxidation products in the reactor effluent were monitored by a CH₃SH sensor, ion chromatography (IC), proton transfer reaction time-of-flight mass spectrometer (PTR-TOFMS).

2.4. Calculation details

DFT calculations were implemented within the Vienna Ab-initio Simulation Package [38–41] (VASP) at the generalized gradient

approximation (GGA) scheme with the PBE exchange-correlation functional [42]. Projector augmented wave (PAW) method [43,44] was selected to model the ion-electron interaction. An energy cutoff of 500 eV was used for the plane-wave basis set expansion, and the Gaussian smearing method was applied, with the σ value chosen to be 0.1 eV. Structures were relaxed until the maximum force on the atoms was smaller than 0.03 eV/Å, and the total energy convergence criterion was set to be 10^{-5} eV for all structure optimizations. During structure optimizations, only Gamma point was sampled. Besides, during single-point calculations for density of states (DOS), a $3 \times 3 \times 1$ Gamma-centered Monkhorst-Pack k points were included for the sampling of Brillouin zone.

3. Results and discussion

We first compared the photocatalytic oxidation of CH₃SH on PCN-MT, which was prepared thermally from Melamine and Trichloroisocyanuric acid, and on PCN-IT, fabricated through IonoThermal polymerization of PCN-MT in KCl/LiCl eutectics. For both photocatalysts, a rapid decrease of CH₃SH concentration is observed upon irradiation in the air atmosphere (Fig. 1a, b). Control experiments show that the reaction cannot proceed without photocatalysts, underlining the important role of PCN catalysts in catalyzing the CH₃SH transformations. These PCN-based catalysts are found to be inactive without light, excluding the possibility of thermocatalytic reaction between CH₃SH and O₂. Additionally, CH₃SH oxidation is demonstrated to be highly oxygen-dependent. Under N₂, the decay of CH₃SH becomes to a much less extent on both photocatalysts, suggesting that the activation of oxygen molecules plays a significant role in CH₃SH oxidation. Experiments for catalysts stability show that there is no obvious decrease in CH₃SH degradation efficiency (Fig. 1c) after 300 min recycling tests. Moreover, XRD and FTIR characterizations of the PCN-MT and PCN-IT before and after the 300 min recycling experiment show that both the crystal structure and the functionalities of photocatalysts is not change much (Fig. S1), demonstrating the excellent stability of these

photocatalysts.

The product analysis by ion chromatography (IC) shows that, on both photocatalysts, the CH₃SO₃H and H₂SO₄ are two main products of the CH₃SH oxidation in the air. The most intriguing difference between the two photocatalysts is their selectivity in CH₃SO₃H and H₂SO₄. On PCN-MT, the dominant product for CH₃SH oxidation is CH₃SO₃H, with a selectivity of 84.0%. Negligible carbon-containing products are detected on PCN-MT. By contrast, on the PCN-IT, H₂SO₄ becomes superior (62.1%). In addition, carbon-containing products including considerable amounts of formic acid (HCOOH), carbonic acid (H₂CO₃) and a small amount of acetic acid (CH₃COOH) are produced (Fig. 1d). These results imply that the methyl groups in CH₃SH are maintained for PCN-MT, while it is oxidized to HCOOH, CH₃COOH and H₂CO₃ for PCN-IT during the photocatalytic oxidation reaction. Variations of CH₃SO₃H and H₂SO₄ during the photocatalytic oxidation of CH₃SH by PCNs are shown in Fig. 1e and f. The total sulfur contents by accounting for these two products are nearly identical to that of eliminated CH₃SH, on both photocatalysts and during the whole reaction process. For PCN-MT, the selectivity of CH₃SO₃H increases slightly at early stage of irradiation (0–60 min), and then becomes constant (84.3%) with further irradiation (Fig. 1e inset). In the previous reports, the oxidation of CH₃SH usually occurs in a sequential manner, that is, CH₃SH is first oxidized to CH₃SO₃H and further transformed to H₂SO₄ [28–31]. This pathway makes it difficult for the reaction to stop at CH₃SO₃H, resulting in low selectivity of CH₃SO₃H. In this work, the observation that the gradual increase in the selectivity of CH₃SO₃H with irradiation time excludes that the sequential reaction is dominant in the oxidation of CH₃SH on PCN-MT. Instead, the formed CH₃SO₃H is difficult to further transform into H₂SO₄ as evidenced by the results from Fig. S2 (details shown in the Supporting Information), thus achieving highly selective production of CH₃SO₃H. On PCN-IT, with H₂SO₄ as dominant product, both the selectivity of H₂SO₄ and CH₃SO₃H keeps constant over the irradiation time. To get more insight into the reaction process, CH₃SH gas was stopped at 15 min but keeping the irradiation to examine if CH₃SO₃H can be further oxidized to H₂SO₄. It is shown from Figure 1f that H₂SO₄ is

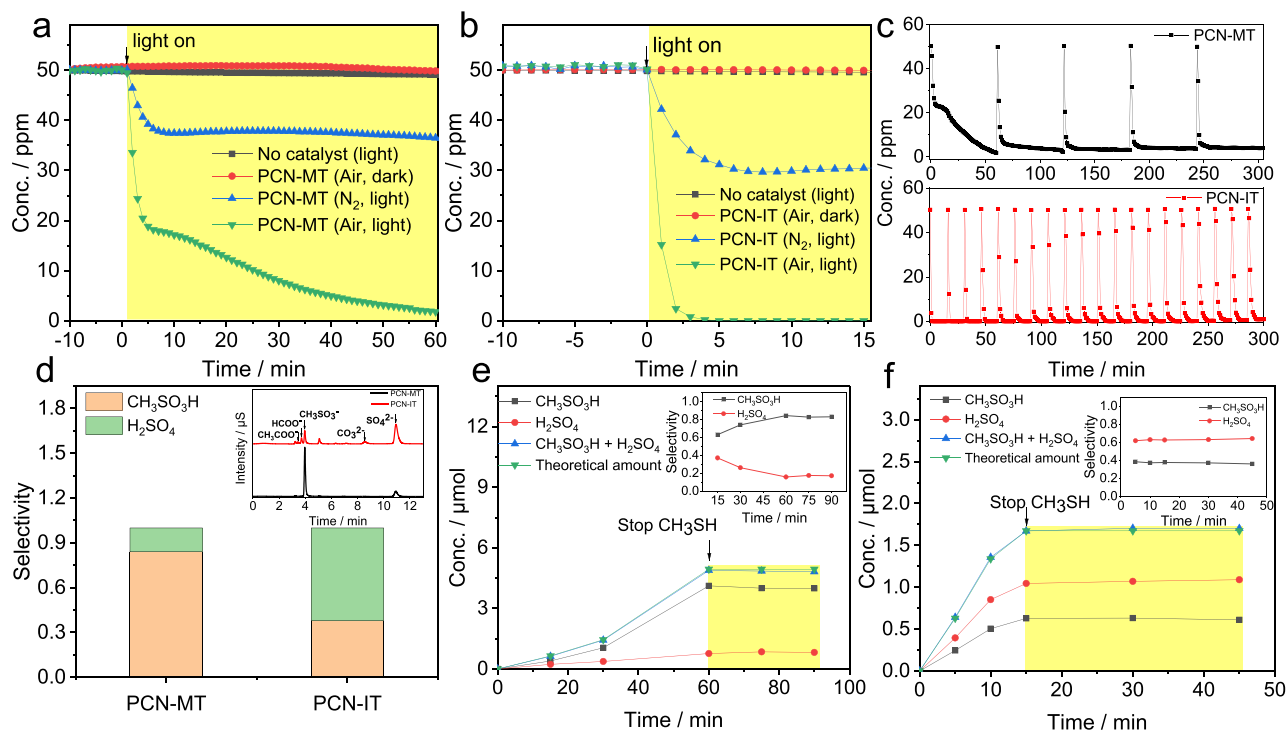


Fig. 1. Photocatalytic performance of PCN-MT (a) and PCN-IT (b) for CH₃SH oxidation under different conditions. (c) Stability test of PCN-MT and PCN-IT. (d) Selectivity of photocatalytic CH₃SH oxidation over PCN-MT and PCN-IT (inset: ion chromatograms for samples of PCN-MT and PCN-IT). Time profiles of sulfur oxides products variation during CH₃SH photocatalytic oxidation over PCN-MT (e) and PCN-IT (f) (inset: sulfur oxides selectivity versus time).

not produced any longer after the stop of CH₃SH, and the amount of CH₃SO₃H is not decreased significantly neither, suggesting that CH₃SO₃H is not the intermediate in CH₃SH to H₂SO₄ conversion catalyzed by PCN-IT. Moreover, when CH₃SO₃H (1.0 μmol) is used as a reactant, negligible H₂SO₄ is produced (Fig. S3), further substantiating that H₂SO₄ is not produced by oxidation of CH₃SO₃H. These results indicate that CH₃SH can be directly converted to H₂SO₄, bypassing the CH₃SO₃H intermediates on PCN-IT. In other words, the H₂SO₄ and CH₃SO₃H during the oxidation of CH₃SH is directly formed on PCN-IT and PCN-MT through two different pathways, respectively. H₂SO₄ selectivity in PCN-IT comes from the oxidation of methyl group in CH₃SH, while the reaction on PCN-MT proceeds via oxidation of S-H bond within CH₃SH to yield CH₃SO₃H.

The identification of the existence of two different oxidation pathways for oxidation of CH₃SH on the PCN-based photocatalyst has important implications. It suggests that product selectivity can be achieved by modulating the occurrence of these two pathways. For this purpose, an understanding of the mechanism of these two pathways is essential. To uncover the underlying reasons for the different behaviors of the two catalysts for photocatalytic CH₃SH aerobic oxidation, we compared the structures of the PCN-MT and PCN-IT samples. Typically, thermal polymerization of melamine yields a one-dimensional (1D) polymer of melon structure [45], whereas ionothermal calcination of melon yields the two-dimensional (2D) poly(heptazine imide) structure [46], which are indicative of the difference in dimensionality between PCN-MT (1D) and PCN-IT (2D). The XRD pattern of PCN-MT (Fig. 2a) shows characteristic peaks at 12.8° and 27.5°, representing in-plane

repeating packing of heptazine units (100) and inter-planar stacking of aromatic segments (002), respectively. With respect to PCN-IT, an obvious shift of the (100) diffraction peak to lower degree (7.8°) could be ascribed to the breakage in the arrangement of in-plane repeating heptazine units in the 2D layer caused by the insertion of K⁺ into the heptazine unit [47,48]. In contrast, the (002) peak of PCN-IT shifts from 27.5° to 28.2° as compared to PCN-MT samples, reflecting a shortened stacking distance of interlayer, and the significantly narrower (002) diffraction peak is indicative of the higher crystallinity in PCN-IT.

Fourier transform infrared (FT-IR) spectroscopies (Fig. 2b) show that both samples exhibit similar characteristic peaks at 810, 1200–1700 and 3000–3500 cm⁻¹, which can be attributed to the out-of-plane bending vibration of heptazine units, stretching and bending vibration of aromatic CN heterocycles, N-H stretching vibration, respectively [49]. Notably, a new peak at 2178 cm⁻¹ appears in PCN-IT, attributed to the cyanamide groups, while this peak is not observable in the PCN-MT sample. On the other hand, the intensity of PCN-MT centered at about 3270 cm⁻¹, which is ascribed to the amino groups, is more significant than that of PCN-IT, implying a relatively higher amount of -NH₂ in PCN-MT. C1s and N 1s XPS spectra were employed to gain further insights of the structural characteristics for these two catalysts. High resolution C 1s spectra of PCN-MT can be deconvoluted into two peaks located at 288.3 and 284.8 eV (Fig. 2c), corresponding to N-C≡N and adventitious hydrocarbon from surroundings, respectively. Note that the C 1s spectrum of PCN-IT display a new peak centered at 286.2 eV, which was reported to be associated with cyanamide-type defects [50], further verifying the existence of -C≡N in PCN-IT. For N 1s spectra

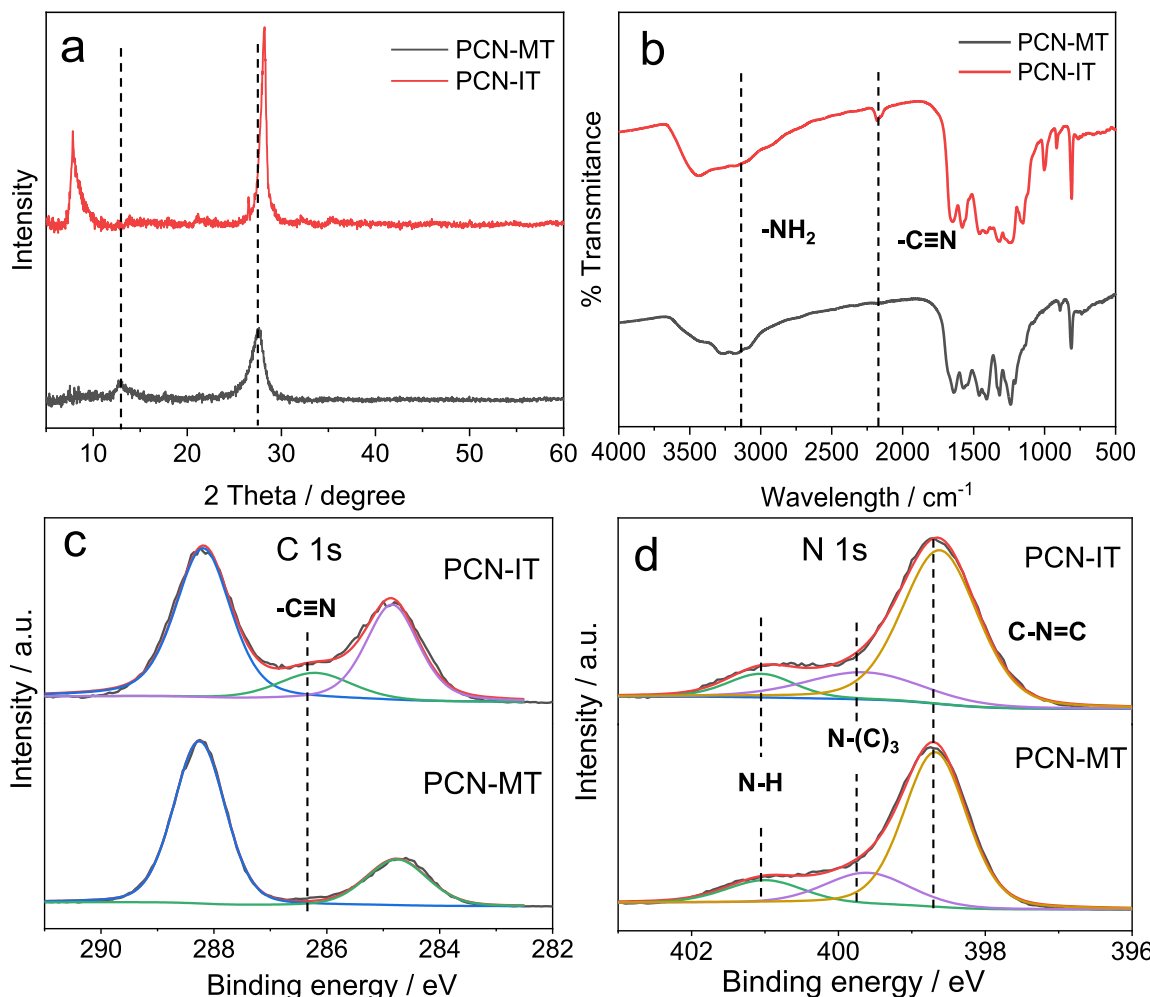


Fig. 2. (a) XRD pattern, (b) FTIR spectra, High resolution of C 1s spectra (c) and N1s (d) spectra of PCN-MT and PCN-IT.

(Fig. 2d), the binding energy peaks at 401.0, 399.6 and 398.7 eV observed for both catalysts are characteristic of amino N (N-H), tertiary N (N-(C)₃) and bi-coordinated N (C-N = C), respectively. The peak area ratios between N-H and N-(C)₃ for PCN-MT and PCN-IT are 0.67 and 0.50, respectively. The distinctly lower value in PCN-IT could be ascribed to the deprotonation of -C-NH₂ in PCN-MT generating cyanamide groups [50]. The above results clearly demonstrate that, besides crystallinity, the two catalysts also possess different edge functional groups. The cyanamide groups on PCN-IT are the major functionals, whereas amino groups are enriched at edge of PCN-MT.

Based on the above results, dimensionality, crystallinity or functional groups in PCN may account for the different products selectivity. To identify the origin of the selectivity differences of PCN on the photocatalytic oxidation of CH₃SH, the edge amino group in PCN-MT was substituted with cyanamide groups by using NaSCN as cyanation reagent, while keeping the 1D polymer backbone (dimensionality) and crystallinity of the catalyst unchanged (Fig. 3a). The successful grafting of cyanamide groups in PCN-MT-2CN was evidenced by the FTIR band (Fig. 3b) at 2178 cm⁻¹, corresponding to C≡N stretching vibrations of cyanamide groups [51], the C1s XPS peak (Fig. S4) at energy of 286.2 eV associated with -C≡N [50], and the ¹³C NMR signal (Fig. S4) centered around 120.4 ppm, which is in accord with previous literature values for potassium melonate [52] and cyanamide-decorated PCN [49,53]. In addition, the cyanamide group content could be readily regulated by varying the NaSCN concentration. When PCN-MT was treated in pure CH₃CN without NaSCN, few cyanamide groups were observed, and the selectivity of H₂SO₄ remains very low, as in the case of original PCN-MT. The treatment of PCN-MT with increased concentration of NaSCN lead to a gradual increase in the contents of cyanamide group. Notably, the H₂SO₄ selectivity augments sharply from 18.2% to 82.0%. These results demonstrate that the cyanamide groups are essential to the formation of H₂SO₄, and that the dimensionality and crystallinity of PCN may present a minor contribution to selectivity. On the other end, to investigate the effects of amino groups on products selectivity, a series of PCN photocatalysts with amino groups were also prepared by different precursors. As shown in Fig. 3d and e, FTIR and XRD spectra confirm the successful

synthesis of the amino rich groups modified PCN photocatalysts with similar crystallinity. It is noteworthy that the selectivity of CH₃SH to CH₃SO₃H for the three catalysts reaches over 78% (Fig. 3f), confirming that edge functional groups make a big difference to the selectivity of CH₃SH oxidation.

To explore the intrinsic reasons for the influence of edge dangling functional units on the selectivity of photocatalytic CH₃SH oxidation, we systematically compared photochemical behaviors of amino- and cyanamide-enriched PCN photocatalysts (PCN-MT-0CN and PCN-MT-2CN), which exhibit very significant differences in product selectivity and functional groups, but possess similar polymer backbone and crystallinity (Fig. 3a and b). Fig. 4a displays the UV-vis diffuse reflectance spectra (DRS) of PCN-MT-0CN and PCN-MT-2CN. The PCN-MT-2CN shows an obvious red-shift with absorption edge extending to ca. 600 nm. The band gap of PCN-MT-0CN and PCN-MT-2CN from the Tauc plots is calculated to be 2.83 and 2.38 eV, respectively. Fig. 4b displays the Mott-Schottky (M-S) plots within frequencies ranging from 0.5 to 1.0 kHz for both samples. The flat band potential determined from the M-S plots for PCN-MT-0CN and PCN-MT-2CN is -1.66 and -0.91 V (vs. NHE), respectively. The valence band (VB) potentials of PCN-MT-0CN and PCN-MT-2CN are accordingly determined to be 1.17 and 1.47 V, respectively. The band structures of the two as-prepared samples are illustrated in Fig. 4c. It can be seen that the introduction of electron-withdrawing terminal -C≡N groups in PCN results in the apparently narrowed band gap, making it adsorb more visible light with lower energy. The downwards shift of the VB position for cyanamide-decorated PCN leads to the stronger oxidizing ability of photo-generated valence band holes.

Photoluminescence spectroscopies including steady-state and time-resolved fluorescence (FL) and phosphorescence (PH) were further investigated to shed light on the charge recombination and separation processes in PCN-MT-0CN and PCN-MT-2CN. As shown in Fig. 4d, FL spectra recorded at ambient temperature exhibits a strong emission peak centered at 506 nm for PCN-MT-0CN, while the emission of PCN-MT-2CN is relatively weak and centered around 538 nm, assigning to radiative decay of singlet excitons. The notable red shift of 32 nm for PCN-

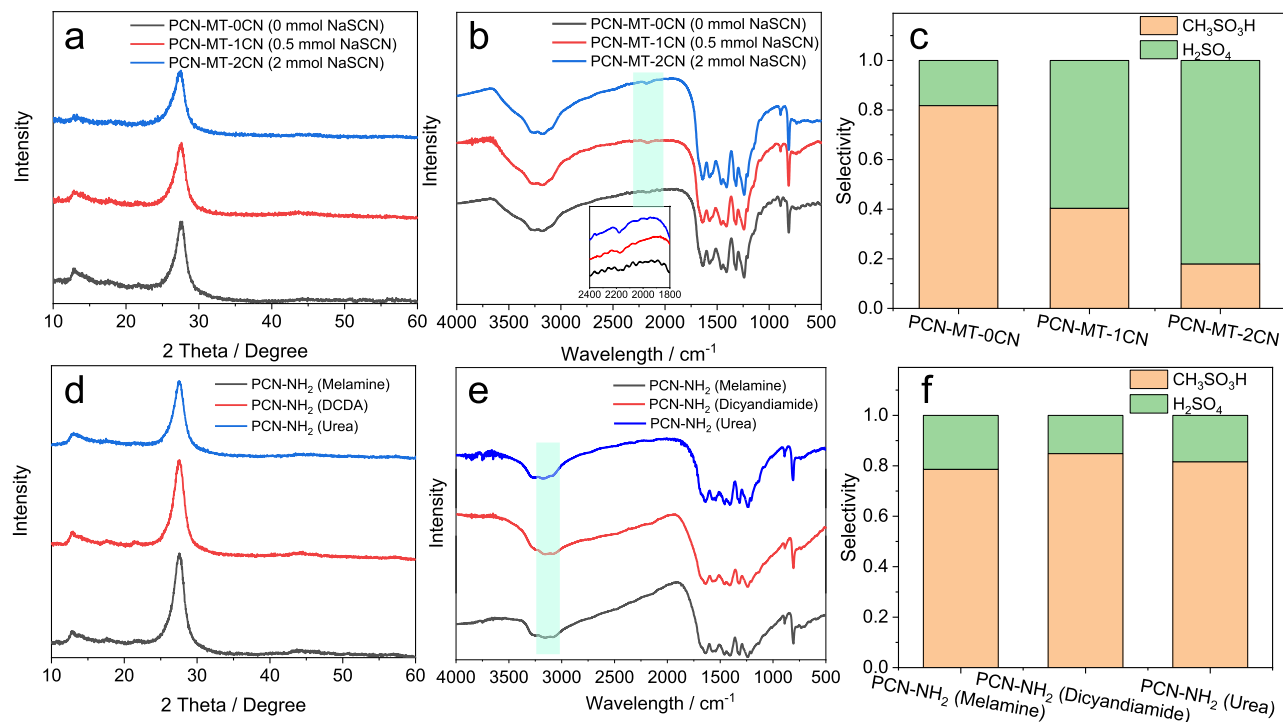


Fig. 3. (a) XRD patterns, (b) FTIR spectra, and (c) selectivity of CH₃SH photocatalytic oxidation over PCN-CN samples, (d) XRD patterns, (e) FTIR spectra, and (f) selectivity of CH₃SH photocatalytic oxidation over as-synthesized PCN-NH₂ samples.

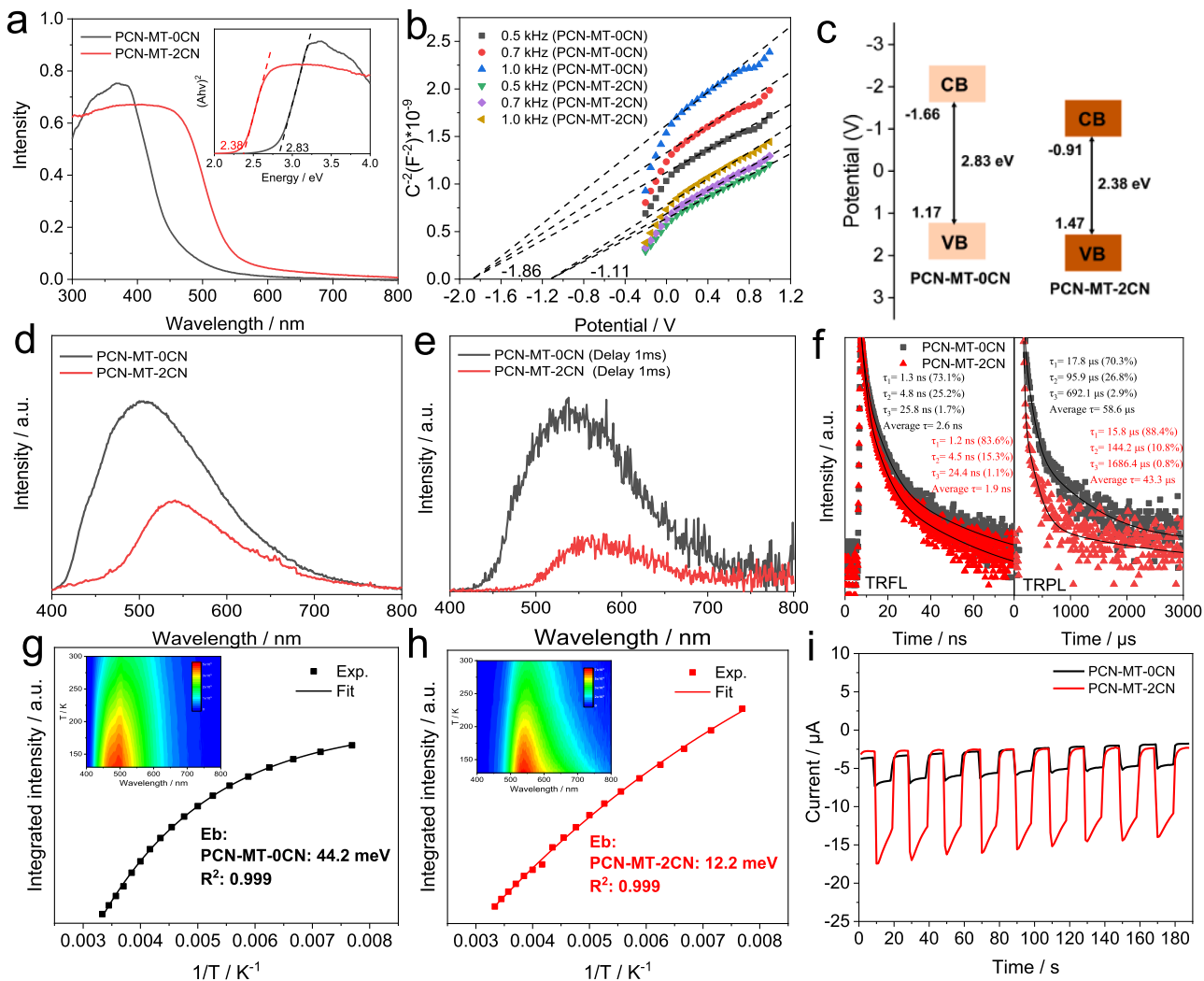


Fig. 4. (a) DRS (inset: Tauc plots), (b) M-S plots and (c) Schematic energetic diagram of PCN-MT-0CN and PCN-MT-2CN. (d) Steady-state FL spectra, (e) PH spectra with delay time of 1 ms, (f) Time-resolved fluorescence (TRFL) and phosphorescence (TRPL) spectra of PCN-MT-0CN and PCN-MT-2CN. Evolution of PL emission intensity as a function of temperature from 130 to 300 K for PCN-MT-0CN (g) and PCN-MT-2CN (h) (inset: Contour plots of the temperature-dependent PL emission spectra). (i) Transient photocurrent response at -0.25 V vs Ag/AgCl.

MT-2CN may arise from its smaller bandgap, which is in good agreement with the DRS results (Fig. 4a). In addition, time-resolved fluorescence (TRFL) measurement was conducted under excitation at 375 nm. As shown in Fig. 4f, the decay profiles can be fitted using treble-exponential decay functions where the shortest lifespan component (τ_1) denotes the electron transfer process between energy levels, the longer (τ_2) and longest one (τ_3) correspond to the nonradiative and radiative recombination, respectively [54]. The treble-exponential fitting for PCN-MT-0CN and PCN-MT-2CN yielded an average lifetime of around 2.6 ns and 1.9 ns, respectively. The weaker FL intensity and shorter lifetime of PCN-MT-2CN suggest the enhanced singlet exciton dissociation and charge transfer in PCN-MT-2CN system. Unlike FL, PH is stemmed from the radiative decay from the triplet excited state to the ground state. As shown in Fig. 4e, the intensity of phosphorescent emission for PCN-MT-0CN sample is stronger than the PCN-MT-2CN one, indicative of a considerably increased population of triplet exciton in the amino-enriched sample. The energy difference between the singlet and triplet states (ΔE_{ST}) obtained by measuring the energy separations between the FL and PH peaks were estimated to evaluate the intersystem crossing (ISC) efficiency [10]. Fig. S5 shows that PCN-MT-0CN with amino defects (0.149 eV) exhibits a slightly smaller ΔE_{ST} with respect to the PCN-MT-2CN counterpart (0.156 eV). The

reduced ISC barrier for PCN-MT-0CN hence dramatically promotes the transformation of singlet exciton into triplet form, resulting in efficient triplet excitons generation. Further, time-resolved phosphorescence spectra (Fig. 4f) of both catalysts exhibit typical multi-stage decay profiles, which was previously reported to be associated with triplet–triplet annihilation, exciton diffusion, or Förster resonance energy transfer [55,56]. Along with triplet concentration decreasing, the decays ultimately turned to monomolecular exponential. The average PH lifetime of PCN-MT-2CN (43.3 μ s) is shorter than PCN-MT-0CN (58.6 μ s), probably resulting from the rapid dissociation of triplet exciton of cyanamide-enriched PCN.

To gain deeper insight into the excitonic process in these two PCN photocatalysts, the exciton binding energy (Eb) were evaluated using temperature-dependent FL spectroscopic measurements. As displayed in the inset of Fig. 4g and h, the FL intensity decreases with the increasing of temperature, which offers the driving force for the singlet exciton dissociation. The corresponding exciton binding energy can be derived by fitting the temperature dependent FL intensity according to the Arrhenius equation [57,58],

$$I(T) = I_0 \left/ \left[1 + A_{\text{exp}} \left(\frac{-E_b}{k_B T} \right) \right] \right.$$

The E_b of PCN-MT-2CN (12.2 mV) is much lower than that of the PCN-MT-0CN case (44.2 mV) (Fig. 4g and h). These results demonstrate that excitonic effects of PCN-MT-0CN are robust, thus resulting in high exciton concentration, whereas the excitons are more easily dissociated into free carriers after introduction of cyanamide units in PCN. The behavior of charge carriers in PCN-MT-0CN and PCN-MT-2CN was then evaluated by photocurrent and electrochemical impedance tests. As shown by Fig. 4i and S6, PCN-MT-2CN exhibits remarkably higher photocurrent response and lower charge-transfer resistance. This confirms that accelerated exciton dissociation in PCN-MT-2CN increases the photogeneration of free charge carriers, giving higher charge migration rate for PCN-MT-2CN. In sharp contrast, the strong excitonic effect of PCN-MT-0CN restricts the number of photogenerated electrons, resulting in weaker photocurrent intensity and larger charge transfer resistance.

Since O_2 is involved in the photocatalytic oxidation reaction of CH_3SH , the formation of reactive oxygen species (ROS) by oxygen activation should greatly affect the photocatalytic selectivity. As the most convincing evidence for the identification of ROS, electron spin resonance (ESR) measurements were carried out to distinguish different photocatalytic active species generated over PCN-MT-0CN and PCN-MT-2CN. As shown in Fig. 5a, we observe the strong and typical 1:1:1 triplet signal of 2,2,6,6-tetramethylpiperidine-N-oxyl (TEMPO) for PCN-MT-0CN when 2,2,6,6-tetramethylpiperidine (TEMP) was used as the 1O_2 probe. The dramatic difference in the intensity of TEMPO signals between the PCN-MT-0CN and PCN-MT-2CN samples clearly reveals the enhanced 1O_2 generation with PCN-MT-0CN. In contrast, by using 5,5-

Dimethyl-1-pyrroline-N-oxide (DMPO) as the trapping agent, the strong sextet ESR signal, which is attributed to the adducts of DMPO and superoxide radical (DMPO-OOH), appears for PCN-MT-2CN sample, whereas very weak DMPO-OOH is observed in the PCN-MT-0CN case. These results indicate that, the amino-enriched PCN tend to photo-activate O_2 by an energy transfer pathway to generate 1O_2 as the dominant ROS, while the PCN with cyanamide-group greatly favors the formation of $\cdot O_2^-$ through an electron transfer process.

To further understand the influence of edge functional groups of PCN on its reactivity, we compared the electronic structures between the two catalysts by DFT calculations. As shown by the density of states (DOS) in Fig. 5c, the energy gap (E_g) between the bottom of conduction band (CB) and the top of valence band (VB) for amino- and cyanamide- grafted PCN are calculated to be 2.27 and 2.17 eV, respectively. Although the E_g values are underestimated somewhat, due to the intrinsic error of the generalized gradient approximation functional in DFT calculations, the E_g of amino-enriched PCN is significantly narrower than that of cyanamide-decorated PCN, which coincides with the UV-vis DRS results (Fig. 4a). An analysis on the DOS also demonstrates that the CB edges for both catalysts are mainly composed of C 2p and N 2p orbitals, while VB edges are dominated by N 2p orbitals (Fig. 5c, d). It is noteworthy that the energy difference (ΔE) between VB edge and the state of CH_3SH derived from S 3p orbitals are quite significant between the two catalysts. For cyanamide decorated PCN catalyst, the state of CH_3SH is located above the VB edge by $\Delta E = 0.73$ eV, while the energy difference for amino-substituted PCN is only 0.22 eV. The larger ΔE in cyanamide-PCN implies that the photogenerated holes have more driving force to

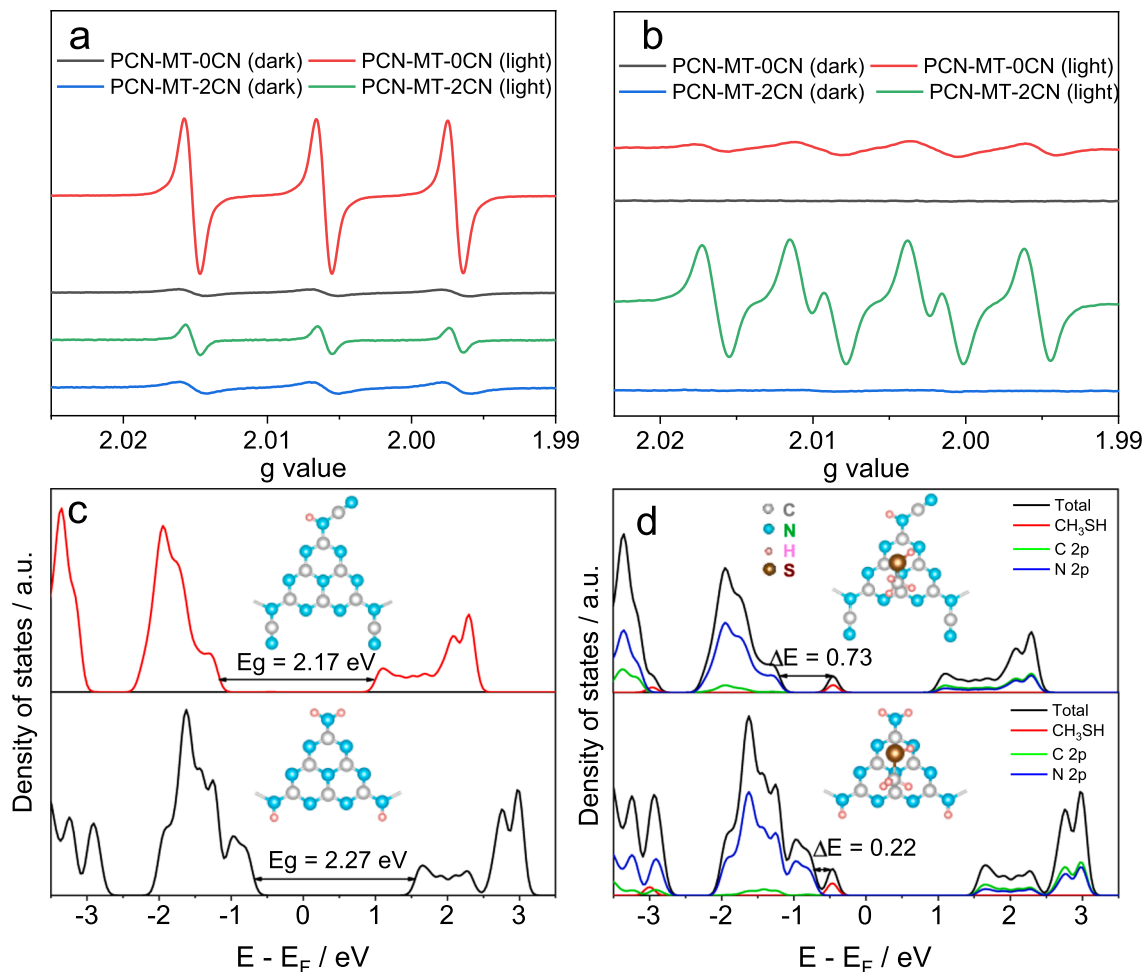


Fig. 5. ESR spectra of (a) TEMP- 1O_2 adducts and (b) DMPO- O_2^- adducts over PCN-MT-0CN and PCN-MT-2CN. (c) Calculated band gap energy for amino- and cyanamide- grafted PCN. (d) Density of states for two PCN catalysts with CH_3SH .

oxide CH_3SH . By contrast, the small ΔE for amino-PCN means that the hole transfer from the VB to CH_3SH is energetically difficult. Such an energetic profile between amino- and cyanamide-PCN is in line with the results from M-S plots. It is evident that the strong electron-withdrawing effect of cyanamide groups makes the VB of cyanamide-PCN possess high oxidation ability, while the substitution of electron-donating amino groups decreases the oxidability.

Based on the aforementioned experimental results, the plausible mechanisms of photocatalytic oxygen of CH_3SH over two PCN are proposed as follows (Fig. 6). For amino moiety enriched PCN, the large exciton binding energy of PCN with NH_2 groups (Fig. 4g), giving rise to strong excitonic effect, restricts the dissociation of excitons. And the small ΔE_{ST} (the energy difference between the singlet and triplet states, Fig. S5) in NH_2 -enriched PCN promotes singlet to triplet exciton transformation, resulting in high population of triplet excitons (Fig. 4e). During the annihilation process of triplets, the energy released could be transferred to the ground state molecular oxygen to generate $^1\text{O}_2$ through resonant energy transfer process. On the other hand, due to the small ΔE between VB edge and the state of CH_3SH (Fig. 5c), charge separation is disfavored so that oxidation of CH_3SH via electron transfer process is difficult to occur. $^1\text{O}_2$ possesses high electrophilicity and shows a considerable reactivity toward electron-rich sites [59–61]. The target molecular CH_3SH contains an electronegative sulfur atom (as compared to carbon), which is sensitive to the electrophilic attack of $^1\text{O}_2$. Thus, singlet-oxygen-driven photocatalytic oxidation of CH_3SH to $\text{CH}_3\text{SO}_3\text{H}$ is dominant in the amino-decorated PCN system. Previously, due to the uncontrollable ROS production, the catalysts generally have a lack of site-selectivity for CH_3SH oxidation, making it difficult for the reaction to stop at $\text{CH}_3\text{SO}_3\text{H}$ and leading to low selectivity for $\text{CH}_3\text{SO}_3\text{H}$. In this work, by virtue of the nonradical nature of $^1\text{O}_2$, high selective production of $\text{CH}_3\text{SO}_3\text{H}$ is achieved through electrophilic addition of $^1\text{O}_2$ to S site within CH_3SH . On the contrary, in the case of cyanated PCN catalyst, the low exciton binding energy (Fig. 4h) results in a high carrier separation efficiency, which limits the $^1\text{O}_2$ generation. By contrast, the large ΔE between VB edge and the state of CH_3SH (Fig. 5d) entail the photogenerated holes possessing strong oxidizing capability to oxide CH_3SH to $\text{CH}_3\text{S}^\cdot$. The high reactivity of $\text{CH}_3\text{S}^\cdot$ renders readily dimerization to form DMDS, which is detected via PTR-TOF-MS (Fig. S7b). Further, the addition of 2,2,6,6-Tetramethylpiperidinoxy (TEMPO), an effective scavenger for thiyl radicals [62,63], into the reaction system, led to a significantly decreased production of DMDS (Fig. S7c), demonstrating that $\text{CH}_3\text{S}^\cdot$ radical is indeed formed in PCN-MT-2CN system. For amino-enriched PCN, little DMDS is observed during the photocatalytic CH_3SH oxidation (Fig. S7a), suggesting little $\text{CH}_3\text{S}^\cdot$ is

generated for NH_2 -decorated PCN due to the preferential reaction of molecular oxygen with the dominant triplet excitons in NH_2 -decorated PCN forming $^1\text{O}_2$. On the other side, the photogenerated electrons are capable of reduce molecular oxygen via electron transfer pathway to produce $\cdot\text{O}_2^-$ species, which subsequently break the $-\text{CH}_3$ end of $\text{CH}_3\text{S}^\cdot$ through hydrogen extraction to produce carbon containing compounds and H_2SO_4 . The formation of $\text{CH}_3\text{S}^\cdot$ and $\cdot\text{O}_2^-$ species indicates that oxidation of CH_3SH on NCN-enriched PCN is a radical-based reaction.

4. Conclusions

In conclusion, excellent tunable site-selectivity of photocatalytic CH_3SH degradation was successfully achieved by regulating edge functional groups of PCN. Due to its strong excitonic effects, the PCN with high density of amino defects prefers to generate $^1\text{O}_2$, which favors electrophilic attacking the $-\text{SH}$ group of CH_3SH and leads to formation of $\text{CH}_3\text{SO}_3\text{H}$. By contrast, due to the low exciton binding energy, cyanation of the amino groups can effectively boost the photogenerated charge separation to produce free holes and electrons. High oxidability of holes enable the activation of CH_3SH to $\text{CH}_3\text{S}^\cdot$, while the free electrons are capable of reducing molecular O_2 to $\cdot\text{O}_2^-$, which prefers to directly damage $-\text{CH}_3$ end of CH_3SH and produce H_2SO_4 and carbon containing compounds. Exploring the role of functional groups in photocatalytic reaction process offer new insight into the structure-selectivity relationship and open a novel avenue for advanced photocatalysts design.

CRediT authorship contribution statement

Shasha Li: Conceptualization, Methodology, Investigation, Data curation, Visualization, Funding acquisition, Writing – original draft. **Yufan Zhang:** Methodology, Data curation, Writing – review & editing. **Youji Li:** Conceptualization, Writing – review & editing. **Jing Xue:** Methodology, Data curation, Writing – review & editing. **Chaoyuan Deng:** Data curation, Visualization. **Wenjing Song:** Conceptualization, Supervision, Writing – review & editing. **Chuncheng Chen:** Conceptualization, Supervision, Funding acquisition, Writing – review & editing. **Jincai Zhao:** Supervision, Funding acquisition, Writing – review & editing.

Declaration of Competing Interest

The authors declare that they have no known competing financial interests or personal relationships that could have appeared to influence the work reported in this paper.

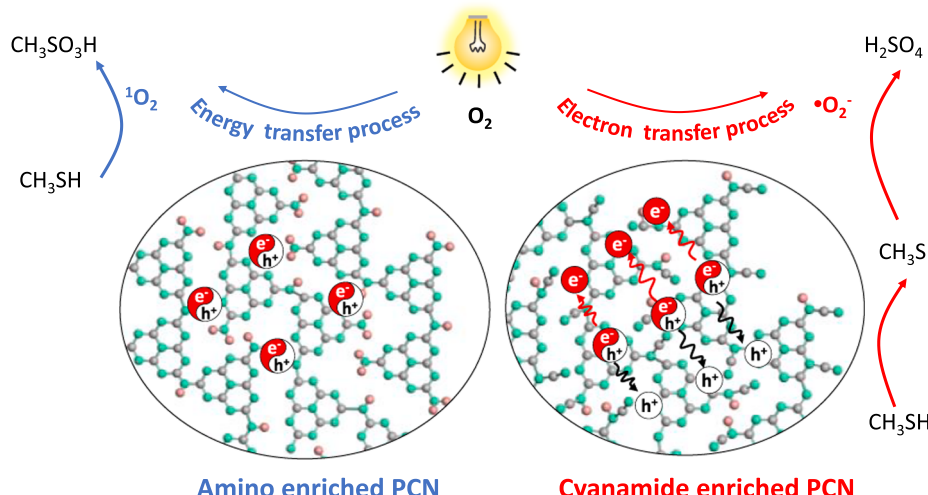


Fig. 6. The mechanism of selective photocatalytic oxidation of CH_3SH induced by tunable molecular oxygen activation.

Data Availability

Data will be made available on request.

Acknowledgments

This work was supported by the Strategic Priority Research Program of Chinese Academy of Sciences, Grant No. XDB36000000, the National Natural Science Foundation of China (Nos. 22136005, 22188102, 22206188), the "National Key R&D Program of China" (No. 2018YFA0209302) and China Postdoctoral Science Foundation (2021M693225).

Appendix A. Supplementary data

Supplementary data includes the catalytic stability characterizations, structural and photoelectrochemical characterizations of PCN, active species verification.

Appendix A. Supporting information

Supplementary data associated with this article can be found in the online version at doi:10.1016/j.apcatb.2023.123180.

References

- [1] F. He, W. Jeon, W. Choi, Photocatalytic air purification mimicking the self-cleaning process of the atmosphere, *Nat. Commun.* 12 (2021) 2528.
- [2] Y. Zhang, Y. Wang, R. Xie, H. Huang, M.K.H. Leung, J. Li, D.Y.C. Leung, Photocatalytic oxidation for volatile organic compounds elimination: From fundamental research to practical applications, *Environ. Sci. Technol.* 56 (2022) 16582–16601.
- [3] K.S. Lakhi, D.-H. Park, K. Al-Bahily, W. Cha, B. Viswanathan, J.-H. Choy, A. Vinu, Mesoporous carbon nitrides: synthesis, functionalization, and applications, *Chem. Soc. Rev.* 46 (2017) 72–101.
- [4] X. Wang, K. Maeda, A. Thomas, K. Takanabe, G. Xin, J.M. Carlsson, K. Domen, M. Antonietti, A metal-free polymeric photocatalyst for hydrogen production from water under visible light, *Nat. Mater.* 8 (2009) 76–80.
- [5] L. Schermermund, S. Reischauer, S. Bierbäumer, C.K. Winkler, A. Diaz-Rodriguez, L. J. Edwards, S. Kara, T. Mielke, J. Cartwright, G. Grogan, B. Pieber, W. Kroutil, Chromoselective photocatalysis enables stereocomplementary biocatalytic pathways, *Angew. Chem. Int. Ed. Engl.* 60 (2021) 6965–6969.
- [6] Y. Dai, C. Li, Y. Shen, T. Lim, J. Xu, Y. Li, H. Niemantsverdriet, F. Besenbacher, N. Lock, R. Su, Light-tuned selective photosynthesis of azo- and azoxy-aromatics using graphitic C(3)N(4), *Nat. Commun.* 9 (2018) 60.
- [7] T. Yang, X. Mao, Y. Zhang, X. Wu, L. Wang, M. Chu, C.W. Pao, S. Yang, Y. Xu, X. Huang, Coordination tailoring of Cu single sites on C(3)N(4) realizes selective CO (2) hydrogenation at low temperature, *Nat. Commun.* 12 (2021) 6022.
- [8] Y. Zhao, P. Zhang, Z. Yang, L. Li, J. Gao, S. Chen, T. Xie, C. Diao, S. Xi, B. Xiao, C. Hu, W. Choi, Mechanistic analysis of multiple processes controlling solar-driven H(2)O(2) synthesis using engineered polymeric carbon nitride, *Nat. Commun.* 12 (2021) 3701.
- [9] Z. Teng, N. Yang, H. Lv, S. Wang, M. Hu, C. Wang, D. Wang, G. Wang, Edge-functionalized g-C(3)N(4) nanosheets as a highly efficient metal-free photocatalyst for safe drinking water, *Chem* 5 (2019) 664–680.
- [10] Z. Zeng, Y. Fan, X. Quan, H. Yu, S. Chen, S. Zhang, Energy-transfer-mediated oxygen activation in carbonyl functionalized carbon nitride nanosheets for high-efficient photocatalytic water disinfection and organic pollutants degradation, *Water Res.* 177 (2020), 115798.
- [11] X.L. Wang, W.Q. Fang, W. Liu, Y. Jia, D. Jing, Y. Wang, L.-Y. Yang, X.-Q. Gong, Y.-F. Yao, H.G. Yang, X. Yao, Brønsted base site engineering of graphitic carbon nitride for enhanced photocatalytic activity, *J. Mater. Chem. A* 5 (2017) 19227–19236.
- [12] F. Li, T. Li, L. Zhang, Y. Jin, C. Hu, Enhancing photocatalytic performance by direct photo-excited electron transfer from organic pollutants to low-polymerized graphitic carbon nitride with more c-NH/NH(2) exposure, *Appl. Catal. B-Environ.* 296 (2021), 120316.
- [13] X. Gao, F. Yang, J. Cheng, Z. Xu, B. Zang, G. Li, X. Xie, W. Luo, Emission of volatile sulphur compounds during swine manure composting: Source identification, odour mitigation and assessment, *Waste Manag.* 153 (2022) 129–137.
- [14] R. Li, Z. Han, H. Shen, F. Qi, M. Ding, C. Song, D. Sun, Emission characteristics of odorous volatile sulfur compound from a full-scale sequencing batch reactor wastewater treatment plant, *Sci. Total Environ.* 776 (2021), 145991.
- [15] Z. Jin, S. Zhang, L. Hu, C. Fang, D. Shen, Y. Long, Effect of substrate sulfur state on MM and DMS emissions in landfill, *Waste Manag.* 116 (2020) 112–119.
- [16] S. Deshmukh, A. Jana, N. Bhattacharyya, R. Bandyopadhyay, R.A. Pandey, Quantitative determination of pulp and paper industry emissions and associated odor intensity in methyl mercaptan equivalent using electronic nose, *Atmos. Environ.* 82 (2014) 401–409.
- [17] C. He, X.-z Li, V.K. Sharma, S.-y Li, Elimination of sludge odor by oxidizing sulfur-containing compounds with ferrate(vi), *Environ. Sci. Technol.* 43 (2009) 5890–5895.
- [18] J. Lu, H. Hao, L. Zhang, Z. Xu, L. Zhong, Y. Zhao, D. He, J. Liu, D. Chen, H. Pu, S. He, Y. Luo, The investigation of the role of basic lanthanum (la) species on the improvement of catalytic activity and stability of HZSM-5 material for eliminating methanethiol-(CH(3)SH), *Appl. Catal. B-Environ.* 237 (2018) 185–197.
- [19] R. Zhang, A. Khalizov, L. Wang, M. Hu, W. Xu, Nucleation and growth of nanoparticles in the atmosphere, *Chem. Rev.* 112 (2012) 1957–2011.
- [20] Y. Zhao, D. Chen, J. Liu, D. He, X. Cao, C. Han, J. Lu, Y. Luo, Tuning the metal-support interaction on chromium-based catalysts for catalytically eliminate methyl mercaptan: Anchored active chromium species through surface hydroxyl groups, *Chem. Eng. J.* 389 (2020), 124384.
- [21] J.M. Estrada, N.J.R.B. Kraakman, R. Muñoz, R. Lebrero, A comparative analysis of odour treatment technologies in wastewater treatment plants, *Environ. Sci. Technol.* 45 (2011) 1100–1106.
- [22] S. Bashkova, A. Bagreev, T.J. Bandosz, Catalytic properties of activated carbon surface in the process of adsorption/oxidation of methyl mercaptan, *Catal. Today* 99 (2005) 323–328.
- [23] S. Bashkova, A. Bagreev, T.J. Bandosz, Adsorption of methyl mercaptan on activated carbons, *Environ. Sci. Technol.* 36 (2002) 2777–2782.
- [24] A. Bagreev, J.A. Menendez, I. Dukhno, Y. Tarasenko, T.J. Bandosz, Oxidative adsorption of methyl mercaptan on nitrogen-enriched bituminous coal-based activated carbon, *Carbon* 43 (2005) 208–210.
- [25] A. Couvert, I. Charron, A. Laplanche, C. Renner, L. Patria, B. Requiem, Treatment of odorous sulphur compounds by chemical scrubbing with hydrogen peroxide—application to a laboratory plant, *Chem. Eng. Sci.* 61 (2006) 7240–7248.
- [26] M.D. Geron, M. Wu, T. Buszta, P. Janney, Environmental benefits of methanesulfonic acid. Comparative properties and advantages, *Green. Chem.* 1 (1999) 127–140.
- [27] F. García-Labiano, L.F. de Diego, A. Cabello, P. Gayán, A. Abad, J. Adánez, G. Sprachmann, Sulphuric acid production via chemical looping combustion of elemental sulphur, *Appl. Energy* 178 (2016) 736–745.
- [28] W. Qu, Z. Tang, W. Liu, Y. Liao, Y. Huang, D. Xia, Q. Lian, S. Tian, C. He, D. Shu, Self-accelerating interfacial catalytic elimination of gaseous sulfur-containing volatile organic compounds as microbubbles in a facet-engineered three-dimensional bioc sponge fenton-like process, *Environ. Sci. Technol.* 56 (2022) 11657–11669.
- [29] Y. Huang, D. Ma, W. Liu, D. Xia, L. Hu, J. Yang, P. Liao, C. He, Enhanced catalytic ozonation for eliminating ch3sh via graphene-supported positively charged atomic Pt undergoing Pt(2+)/Pt(4+) redox cycle, *Environ. Sci. Technol.* 55 (2021) 16723–16734.
- [30] C. He, Y. Wang, Z. Li, Y. Huang, Y. Liao, D. Xia, S.C. Lee, Facet engineered α -MnO (2) for efficient catalytic ozonation of odor CH(3)SH: oxygen vacancy-induced active centers and catalytic mechanism, *Environ. Sci. Technol.* 54 (2020) 12771–12783.
- [31] D. Xia, W. Xu, Y. Wang, J. Yang, Y. Huang, L. Hu, C. He, D. Shu, D.Y.C. Leung, Z. Pang, Enhanced performance and conversion pathway for catalytic ozonation of methyl mercaptan on single-atom Ag deposited three-dimensional ordered mesoporous MnO(2), *Environ. Sci. Technol.* 52 (2018) 13399–13409.
- [32] J. Yang, Y. Huang, Y.-W. Chen, D. Xia, C.-Y. Mou, L. Hu, J. Zeng, C. He, P.K. Wong, H.-Y. Zhu, Active site-directed tandem catalysis on cuo/vo-mno2 for efficient and stable catalytic ozonation of S-VOCs under mild condition, *Nano Today* 35 (2020), 100944.
- [33] J. Yang, Q. Zhang, F. Zhang, D. Xia, H. Liu, S. Tian, L. Sun, D. Shu, C. He, S. Runa, Three-dimensional hierarchical porous sludge-derived carbon supported on silicon carbide foams as effective and stable fenton-like catalyst for odorous methyl mercaptan elimination, *J. Hazard. Mater.* 358 (2018) 136–144.
- [34] M. Xie, W. Wei, Z. Jiang, Y. Xu, J. Xie, Carbon nitride nanowires/nanofibers: a novel template-free synthesis from a cyanuric chloride–melamine precursor towards enhanced adsorption and visible-light photocatalytic performance, *Ceram. Int.* 42 (2016) 4158–4170.
- [35] X. Chen, R. Shi, Q. Chen, Z. Zhang, W. Jiang, Y. Zhu, T. Zhang, Three-dimensional porous g-C(3)N(4) for highly efficient photocatalytic overall water splitting, *Nano Energy* 59 (2019) 644–650.
- [36] L. Lin, H. Ou, Y. Zhang, X. Wang, Tri-s-triazine-based crystalline graphitic carbon nitrides for highly efficient hydrogen evolution photocatalysis, *ACS Catal.* 6 (2016) 3921–3931.
- [37] L. Li, D. Cruz, A. Savateev, G. Zhang, M. Antonietti, Y. Zhao, Photocatalytic cyanation of carbon nitride scaffolds: tuning band structure and enhancing the performance in green light driven C-S bond formation, *Appl. Catal. B-Environ.* 229 (2018) 249–253.
- [38] G. Kresse, J. Hafner, Ab initio molecular dynamics for liquid metals, *Phys. Rev. B* 47 (1993) 558–561.
- [39] G. Kresse, J. Hafner, Ab initio molecular-dynamics simulation of the liquid-metal-amorphous-semiconductor transition in germanium, *Phys. Rev. B* 49 (1994) 14251–14269.
- [40] G. Kresse, J. Furthmüller, Efficiency of ab-initio total energy calculations for metals and semiconductors using a plane-wave basis set, *Comp. Mater. Sci.* 6 (1996) 15–50.
- [41] G. Kresse, J. Furthmüller, Efficient iterative schemes for ab initio total-energy calculations using a plane-wave basis set, *Phys. Rev. B* 54 (1996) 11169–11186.
- [42] J.P. Perdew, K. Burke, M. Ernzerhof, Generalized gradient approximation made simple, *Phys. Rev. Lett.* 77 (1996) 3865–3868.

[43] P.E. Blöchl, Projector augmented-wave method, *Phys. Rev. B* 50 (1994) 17953–17979.

[44] G. Kresse, D. Joubert, From ultrasoft pseudopotentials to the projector augmented-wave method, *Phys. Rev. B* 59 (1999) 1758–1775.

[45] F.K. Kessler, Y. Zheng, D. Schwarz, C. Merschjann, W. Schnick, X. Wang, M. J. Bojdys, Functional carbon nitride materials - design strategies for electrochemical devices, *Nat. Rev. Mater.* 2 (2017) 17030.

[46] Z. Chen, A. Savateev, S. Pronkin, V. Papaeftithimou, C. Wolff, M.G. Willinger, E. Willinger, D. Neher, M. Antonietti, D. Dontsova, "The easier the better" preparation of efficient photocatalysts-metastable poly(heptazine imide) salts, *Adv. Mater.* 29 (2017), 1700555.

[47] C. Qiu, Y. Xu, X. Fan, D. Xu, R. Tandiana, X. Ling, Y. Jiang, C. Liu, L. Yu, W. Chen, C. Su, Highly crystalline K-intercalated polymeric carbon nitride for visible-light photocatalytic alkenes and alkynes deuterations, *Adv. Sci.* 6 (2019), 1801403.

[48] G. Zhang, L. Lin, G. Li, Y. Zhang, A. Savateev, S. Zafeiratos, X. Wang, M. Antonietti, Ionothermal synthesis of triazine-heptazine-based copolymers with apparent quantum yields of 60% at 420nm for solar hydrogen production from "sea water", *Angew. Chem. Int. Ed. Engl.* 57 (2018) 9372–9376.

[49] L. Chen, C. Chen, Z. Yang, S. Li, C. Chu, B. Chen, Simultaneously tuning band structure and oxygen reduction pathway toward high-efficient photocatalytic hydrogen peroxide production using cyano-rich graphitic carbon nitride, *Adv. Funct. Mater.* 31 (2021), 2105731.

[50] W. Wang, H. Zhang, S. Zhang, Y. Liu, G. Wang, C. Sun, H. Zhao, Potassium-ion-assisted regeneration of active cyano groups in carbon nitride nanoribbons: Visible-light-driven photocatalytic nitrogen reduction, *Angew. Chem. Int. Ed. Engl.* 58 (2019) 16644–16650.

[51] J. Sophia, D. Makowski, J. Gunzelmann, W. Senker, Schnick, Protonated melonate Ca[HC₆N₇(NCN)₃]·7H₂O - synthesis, crystal structure, and thermal properties, *Z. Anorg. Allg. Chem.* 635 (2009) 2434–2439.

[52] E. Horvath-Bordon, E. Kroke, I. Svoboda, H. Fuess, R. Riedel, Potassium melonate, K₃[C₆N₇(NCN)₃]·5H₂O, and its potential use for the synthesis of graphite-like C (3)N(4) materials, *N. J. Chem.* 29 (2005) 693–699.

[53] H. Schlobberg, J. Kröger, G. Savasci, M.W. Terban, S. Bette, I. Moudrakovski, V. Duppel, F. Podjaski, R. Siegel, J. Senker, R.E. Dinnebier, C. Ochsenfeld, B. V. Lotsch, Structural insights into poly(heptazine imides): a light-storing carbon nitride material for dark photocatalysis, *Chem. Mater.* 31 (2019) 7478–7486.

[54] Y. Wang, K. Wang, F. Dai, K. Zhang, H. Tang, L. Wang, J. Xing, A warm-white light-emitting diode based on single-component emitter aromatic carbon nitride, *Nat. Commun.* 13 (2022) 6495.

[55] H. Wang, S. Jiang, W. Liu, X. Zhang, Q. Zhang, Y. Luo, Y. Xie, Ketones as molecular co-catalysts for boosting exciton-based photocatalytic molecular oxygen activation, *Angew. Chem. Int. Ed. Engl.* 59 (2020) 11093–11100.

[56] H. Wang, S. Jiang, S. Chen, D. Li, X. Zhang, W. Shao, X. Sun, J. Xie, Z. Zhao, Q. Zhang, Y. Tian, Y. Xie, Enhanced singlet oxygen generation in oxidized graphitic carbon nitride for organic synthesis, *Adv. Mater.* 28 (2016) 6940–6945.

[57] L. Zhu, J. Zhang, Y. Guo, C. Yang, Y. Yi, Z. Wei, Small exciton binding energies enabling direct charge photogeneration towards low-driving-force organic solar cells, *Angew. Chem. Int. Ed. Engl.* 60 (2021) 15348–15353.

[58] G. Chen, Z.D. Zhang, Y.X. Liao, Z. Zhang, Y.Z. You, Modulating local charge distribution of carbon nitride for promoting exciton dissociation and charge-induced reactions, *Small* 17 (2021), e2100698.

[59] G.G. Kramarenko, S.G. Hummel, S.M. Martin, G.R. Buettner, Ascorbate reacts with singlet oxygen to produce hydrogen peroxide, *Photochem. Photobiol.* 82 (2006) 1634–1637.

[60] R. Zhang, Y. Liu, Z. Wang, P. Wang, Z. Zheng, X. Qin, X. Zhang, Y. Dai, M.-H. Whangbo, B. Huang, Selective photocatalytic conversion of alcohol to aldehydes by singlet oxygen over bi-based metal-organic frameworks under UV-Vis light irradiation, *Appl. Catal. B-Environ.* 254 (2019) 463–470.

[61] Q. Qi, Y. Li, H. Liu, B. Li, H. Wang, Y. Lu, W. Gao, Y. Tian, B. Guo, X. Jia, J. Chen, Alkali metal modified carbon nitride enhance photocatalytic performance for highly selective oxidation of benzyl C(sp³)-H bonds, *Appl. Catal. B-Environ.* 319 (2022), 121864.

[62] L. Xu, X. Deng, Z. Li, Photocatalytic splitting of thiols to produce disulfides and hydrogen over PtS/ZnIn₂S₄ nanocomposites under visible light, *Appl. Catal. B-Environ.* 234 (2018) 50–55.

[63] Y. Yuan, Y. Chen, S. Tang, Z. Huang, A. Lei, Electrochemical oxidative oxysulfenylation and aminosulfenylation of alkenes with hydrogen evolution, *Sci. Adv.* 4 (2018) eaat5312.